Materials Today Bio 27 (2024) 101147

Contents lists available at ScienceDirect

Materials Today Bio

journal homepage: www.journals.elsevier.com/materials-today-bio

Synergistic effect of ultrasound and reinforced electrical environment by bioinspired periosteum for enhanced osteogenesis via immunomodulation of macrophage polarization through Piezo1

Ting Jiang [a,b,1], Fei Yu [c,1], Yuqi Zhou [d,1], Ruomei Li [a,b], Mengting Zheng [b], Yangyang Jiang [a], Zhenxia Li [a,**], Jun Pan [e,***], Ningjuan Ouyang [a,*]

[a] Department of Orthodontics, Shanghai Ninth People's Hospital, Shanghai Jiao Tong University School of Medicine, College of Stomatology, Shanghai Jiao Tong University, National Center for Stomatology, National Clinical Research Center for Oral Diseases, Shanghai Key Laboratory of Stomatology, Research Unit of Oral and Maxillofacial Regenerative Medicine, Chinese Academy of Medical Sciences, Shanghai, 200011, China
[b] Oral Bioengineering Lab, Shanghai Key Laboratory of Stomatology & Shanghai Research Institute of Stomatology, Shanghai, 200011, China
[c] State Key Laboratory of Oral Diseases, National Center for Stomatology, National Clinical Research Center for Oral Diseases, Department of Orthodontics, West China Hospital of Stomatology, Sichuan University, Chengdu, Sichuan, China
[d] Department of Stomatology, Weifang People's Hospital Stomatological Hospital, Weifang, 261041, China
[e] School of Physical and Mathematical Sciences, Nanyang Technological University, Singapore, 637371, Singapore

ARTICLE INFO

Keywords:
LIPUS
Piezoelectric periosteum
Electrical environment
Macrophage
Osteogenesis

ABSTRACT

The periosteum plays a vital role in repairing bone defects. Researchers have demonstrated the existence of electrical potential in the periosteum and native bone, indicating that electrical signals are essential for functional bone regeneration. However, the clinical use of external electrical treatments has been limited due to their inconvenience and inefficacy. As an alternative, low-intensity pulsed ultrasound (LIPUS) is a noninvasive form of physical therapy that enhances bone regeneration. Furthermore, the wireless activation of piezoelectric biomaterials through ultrasound stimulation would generate electric charges precisely at the defect area, compensating for the insufficiency of external electrical stimulation and potentially promoting bone regeneration through the synergistic effect of mechanical and electrical stimulation. However, the optimal integration of LIPUS with an appropriate piezoelectric periosteum is yet to be explored. Herein, the $BaTiO_3$/multiwalled-carbon nanotubes/collagen (BMC) membranes have been fabricated, possessing physicochemical properties including improved surface hydrophilicity, enhanced mechanical performance, ideal piezoelectricity, and outstanding biocompatibility, all of which are conducive to bone regeneration. When combined with LIPUS, the endogenous electrical microenvironment of native bone was recreated. After that, the wireless-generated electrical signals, along with the mechanical signals induced by LIPUS, were transferred to macrophages and activated Ca^{2+} influx through Piezo1. Ultimately, the regenerative effect of the BMC membrane with LIPUS stimulation (BMC + L) was confirmed in a mouse cranial defect model. Together, this research presents a co-engineering strategy that involves fabricating a novel biomimetic periosteum and utilizing the synergistic effect of ultrasound to enhance bone regeneration, which is achieved through the reinforcement of the electrical environment and the immunomodulation of macrophage polarization.

1. Introduction

The periosteum is crucial in the repair of bone defects as it supplies the necessary substances and cells for osteogenesis. It contributes to more than 70 % of *de novo* bone formation at the initial stage of bone repair mediated by autografts [1,2]. However, an insufficient or

* Corresponding author.
** Corresponding author.
*** Corresponding author.
E-mail addresses: lizhenxiairis@163.com (Z. Li), jun.pan@ntu.edu.sg (J. Pan), oynjc0508@163.com (N. Ouyang).
[1] These authors contributed equally.

https://doi.org/10.1016/j.mtbio.2024.101147
Received 21 April 2024; Received in revised form 18 June 2024; Accepted 3 July 2024
Available online 5 July 2024

dysfunctional periosteum can impede bone regeneration, resulting in delayed healing or permanent deformities, which has become a major clinical challenge [3]. Bone regeneration is a complex and highly coordinated process requiring bioelectrical, mechanical, and other physiological cues. Despite these requirements, conventional tissue-engineered periosteum often falls short of fulfilling these functions. This is because it either merely mimics the periosteum through structural design or relies on the delivery of cytokines, which may not be sufficient to replicate the native periosteum's complex role in bone healing [4].

It is worth noting that the functional activities of bone reconstruction require electrical signals. Researchers have demonstrated the existence of electrical potential in both the periosteum and native bone [5]. This electrical potential is typically reduced at the site of bone fracture and gradually returned to its normal level during fracture healing, indicating that the restoration of this diminished bioelectrical environment could enhance bone regeneration [6]. Clinically, various forms of external electrical stimulation have been acknowledged as effective methods for facilitating bone healing and addressing nonunion fractures [7]. However, the widespread clinical application of these electrical treatments has been hindered by several limitations [8]. Firstly, the application of electrical stimulation often involves invasive procedures, such as the subcutaneous implantation of electrodes, which increases the risk of infection. Secondly, the materials used in electrodes or electroacupuncture for electrical stimulation are typically metallic, which may lead to potential long-term side effects. Thirdly, additional elastic or morphing materials are required since the electronic devices used to generate electrical stimulation cannot provide a precise connection to the targeted tissue [9].

As an alternative, low-intensity pulsed ultrasound (LIPUS) is a noninvasive form of mechanical stimulation that utilizes high-frequency pressure waves to accelerate tissue healing and promote bone regeneration [10]. Recognized for its clinical efficacy, the US Food and Drug Administration (FDA) approved LIPUS for the treatment of fresh fractures and bone nonunion in 1994 and 2000, respectively [11]. LIPUS is valued for its noninvasiveness, proven efficacy, safety, precision, user-friendly operation, and brief treatment duration [12]. Moreover, the wireless activation of piezoelectric biomaterials through ultrasound stimulation offers the potential to generate electric charges directly at the defect site, compensating for the limitations of external electrical stimulation, and is hypothesized to significantly promote bone regeneration through the synergistic effect of mechanical and electrical stimulation. Yet, the optimal integration of LIPUS with a suitable piezoelectric periosteum is an area that requires further exploration.

In this study, to explore a biomimetic periosteum with ideal physicochemical properties and biological functions, multi-walled carbon nanotubes (MWCNTs) were utilized due to the suitable mechanical properties to withstand compressive forces encountered during bone repair [13]. Additionally, the incorporation of water-soluble MWCNTs with hydrophilic groups would contribute to improved biocompatibility [14,15]. The integration of Barium titanate (BaTiO3, BT) was a strategic choice to significantly boost the piezoelectric properties of the biomimetic periosteum [16]. Furthermore, to replicate the natural composition and structure, we employed type I collagen (Col), the primary organic component of the periosteum and bone matrix, which contributes to the toughness of the tissue and offers a conducive microenvironment for cell attachment and growth [17]. Consequently, the combination of BT, MWCNTs, and Col to create a bioactive periosteum that is sensitive to ultrasonic stimulation is a compelling approach. This composite is designed to convert the mechanical signal of LIPUS into wireless electrical stimulation, thereby potentially enhancing bone regeneration through synergistic mechanical and electrical stimulation.

In addition to emulating the natural periosteum's function, biomaterial scaffolds designed for efficient osteoinduction should also provide an immunomodulatory effect. It has been demonstrated that the monocyte/macrophage lineage plays a critical role in acute inflammatory responses to biomaterials and bone regeneration [18]. This is attributed to their significant plasticity in response to environmental signals and their diverse functions in maintaining bone homeostasis [19]. Proinflammatory 'M1' macrophages are instrumental in early angiogenesis while alternatively activated 'M2' macrophages contribute to anti-inflammatory processes and support tissue healing [20]. Although there has been a growing interest in how physical signals regulate immune cells, few studies have specifically addressed how electrical signals or LIPUS individually modulate macrophage polarization. To our knowledge, no research has yet explored the synergistic effects of these stimuli on macrophages through a biomimetic periosteum [21].

In this work, inspired by the phenomenon that electrical stimulation promotes osteogenesis, we have developed a wireless piezoelectric stimulation system. To achieve this, we employed the co-engineering strategy by constructing a biomimetic periosteum based on BT/MWCNTs/Col (BMC) and utilizing the synergistic effect of LIPUS to enhance bone regeneration through the reinforced electrical environment and immunomodulation of macrophage polarization. The results demonstrated that the BMC membrane exhibited a range of desired physicochemical functions including improved surface hydrophilicity, mechanical performance, piezoelectricity, biocompatibility, all of which are conducive to bone regeneration. By combining the BMC membrane with LIPUS, we were able to recreate the endogenous electrical microenvironment similar to that of native bone. Subsequently, the wireless-generated electrical signals, along with the mechanical signals induced by LIPUS, were transferred to macrophages, leading to the activation of Ca^{2+} influx through Piezo1 channels. Ultimately, we confirmed the regenerative effect of the BMC membrane with LIPUS stimulation (BMC + L) in a mouse cranial defect model. This research presents a promising co-engineering strategy for bone regeneration by integrating a novel biomimetic periosteum with the synergistic effects of ultrasound, thereby enhancing the electrical environment and modulating macrophage polarization.

2. Materials and methods

2.1. Fabrication and characterization of the BMC membranes

First, 0.1 g of BT (100 nm, Shanghai Macklin Biochemical Co., Shanghai, China) was dispersed in 5 g of 0.2 % MWCNT aqueous dispersion (10 % MWCNT water dispersion), and 50 ml of water was added. Then, to prepare the BMC membrane, 0.08 g of Col (Shanghai Macklin Biochemical Co., Shanghai, China) was added and sonicated for 20 min to disperse the solution. Next, it was filtered to form a membrane and dried at room temperature for further use. The BM ($BaTiO_3$/MWCNTs) membrane and the MC (MWCNTs/Col) membranes were fabricated using the same method.

XRD patterns were collected by a powder diffractometer (Bruker D8 Adv., Cu kα radiation, λ = 1.5418 Å, Germany). Raman spectra were collected from a Horiba LabRAM HR spectrometer. The water contact angle was measured using a Dataphysics OCA20 CA measuring instrument (DataPhysics Instruments GHPH, Filderstadt). SEM images were acquired using a field-emission scanning electron microscope (HITACHI S4800, Japan). The mechanical properties, such as nanoindentation hardness and Young's moduli, were characterized via nanoindentation using a Bruker Hysitron TI980 (Bruker). The piezoelectric coefficient (d33) was recorded on a piezoelectric coefficient meter (ZJ-3A, Insitute of Acoustics, Chinese Academy of Sciences, Beijing, China). The real-time output voltage of various membranes with or without LIPUS stimulation was recorded by an oscilloscope (Tektronix MDO-3034, USA).

2.2. Cell culture and LIPUS treatment

Primary bone marrow mesenchymal stem cells (BMSCs) were

derived from male C57/BL6 mice (3 weeks of age). BMSCs were flushed from long bones and resuspended in αMEM medium with 10 % fetal bovine serum and 1 % penicillin-streptomycin mixture. RAW264.7 macrophage cell line was obtained from the American Type Culture Collection (ATCC, USA) and cultured in αMEM medium.

In vitro, BMC membranes were placed in cell culture plates and connected to an ultrasonic generator via a custom-made mold with conductive gel. The LIPUS stimulation parameters were set at 1.5 MHz, 45 mW/cm^2, and 20 min, and stimulation was produced by an ultrasonic generator. LIPUS was applied once a day, and a parallel group of untreated cells on the culture dish was used as a control. In vivo, the defects were covered by the BMC membranes immediately after surgery, and LIPUS treatment was performed once a day.

2.3. Cell counting kit-8 assay 8 (CCK-8)

Biocompatibility of the BMC membranes was evaluated through BMSCs viability assessment. BMSCs were cultured on BMC membranes in 96-well microplates at a density of 5×10^3 cells per well. Subsequently, the culture medium was substituted with 100 μl of serum-free αMEM medium supplemented with 10 % CCK-8 solution. Following an incubation period of 1 h at 37 °C, the optical density was measured at a wavelength of 450 nm using a microplate reader.

2.4. Live/dead cell staining

After culturing on BMC membranes in 24-well microplates at an initial density of 10^4 cells per well, live and dead cells were stained with a calcein-AM/PI staining kit (C2015S; Beyotime, China) and observed under a Zeiss Axiovert 400 microscope (Zeiss, Germany).

2.5. Immunofluorescence staining

After washing with phosphate buffer solution (PBS), cells underwent fixation using 4 % paraformaldehyde, followed by permeabilization using a 0.1 % Triton X-100 solution for 15 min. Subsequently, they were treated with 5 % bovine serum albumin (BSA) for 1 h to prevent nonspecific binding. Thereafter, cells were incubated with antibodies against OCN (AF6297, Beyotime, China), iNOS (ab3523, Abcam, USA), CD163 (ab182422, Abcam, USA), OPN (AF7665, Beyotime, China), Piezo1 (NBP1-78537, NOVUS, USA) and F-actin (TRITC-phalloidin, 40736ES75, Yeasen, China) at 4 °C overnight, followed by fluorescent secondary antibodies for 2 h at room temperature as previously described [22]. Cell nuclei were identified with DAPI (C1006, Beyotime, China). Fluorescent labeling was analyzed using a fluorescent upright microscope (BX51, Olympus). Fluorescence intensities were evaluated using ImageJ software.

In specific experiments, GsMTx4 (ab141871, Abcam, USA) was used to block the Piezo1 channel.

2.6. Real-time quantitative polymerase chain reaction (Rt-qPCR)

Total RNA was isolated using TRIzol reagent (Invitrogen, New York, USA), followed by reverse transcription using the PrimeScript RT reagent kit (Takara, Dalian, China). Subsequently, real-time quantitative PCR (Rt-qPCR) was conducted on a LightCycler 480 II (Roche) utilizing SYBR Green Mix (Takara, Dalian, China). Data analysis employed the comparative cycle threshold method (ΔΔCt), with normalization against the housekeeping gene GAPDH. Primer sequences utilized for amplification are detailed in Table 1.

2.7. ALP staining and quantitation

ALP staining was performed on BMSCs with commercial kits (Beyotime, Shanghai, China) according to the manufacturer's instructions. A semiquantitative analysis of the ALP activity of BMSCs was performed by using the ALP assay kit (Beyotime, Shanghai, China). The total protein was measured using a bicinchoninic acid (BCA) assay kit (A045-4-2, Nanjing Jiancheng Bioengineering Institute, China).

2.8. Flow cytometry

Cells were harvested and then washed and resuspended in PBS, blocked with anti-FcRII/III antibody for 30 min, and stained with antibodies against CD86 (105,014, Biolegend, USA), CD206 (321,109, Biolegend, USA) according to the manufacturer's protocol. Dead cells were distinguished utilizing the Fixable Viability Stain 700 (FVS700, BD Biosciences). Subsequently, the immunostained and unstained cells were analyzed utilizing a flow cytometer (Beckman Navios, USA) and processed with FLOWJO software (Tree Star, San Carlos, CA, USA).

2.9. Western blot

RAW 264.7 cells were collected with RIPA buffer and then centrifuged at 12,000 rpm at 4 °C to obtain total protein. Western blot analysis was performed as previously described with iNOS (1:1000, ab3523, Abcam, USA), CD163 (1:500, ab182422, Abcam, USA), and GAPDH (1:5000, D16H11, Cell Signaling Tech Inc., USA) [23].

2.10. ARS staining and quantitation

After culturing for 14 days, ARS staining and quantitative analysis were performed on BMSCs with commercial kits (Beyotime, Shanghai, China) according to the manufacturer's instructions.

2.11. Calvarial defect model

The mouse experiments were approved by the Ethics Review Board at the Shanghai Ninth Peoples Hospital (Shanghai, China; SH9H-2022-A41-1). Male C57/BL6 mice (6 weeks of age) were anesthetized to establish a calvarial defect model (5 mm in diameter). Then, the BMC

Table 1
Primer sequences for qRT-PCR.

	Forward	Reverse
GAPDH	CCCCACACACATGCACTTACC	CCTACTCCCAGGGCTTTGATT
ALP	ACACTCGGCCGATCGGGACT	CCGCCACCCATGATCACGTCG
Runx2	ATCGCCTCAGTGATTTAGGG	TGCCTGGGATCTGTAATCTG
OCN	TAGTGAACAGACTCCGGCGCTA	TGTAGGCGGTCTTCAAGCCAT
OPN	GGTGATAGCTTGGCTTATGGACTG	GCTCTTCATGTGAGAGGTGAGGTC
TNFα	ATGTCTCAGCCTCTTCTCATTC	GCTTGTCACTCGAATTTTGAGA
IL-1β	GTGGCTGTGGAGAAGCTGTG	GAAGGTCCACGGGAAAGACAC
iNOS	GTTCTCAGCCCAACAATACAAGA	GTGGACGGGTCGATGTCAC
CD206	CCTATGAAAATTGGGCTTACGG	CTGACAAATCCAGTTGTTGAGG
Arg1	TCACCTGAGCTTTGATGTCG	CTGAAAGGAGCCCTGTCTTG
Col I	GAGCGGAGAGTACTGGATCG	GTTCGGGCTGATGTACCAGT

membranes were implanted into mice to evaluate the osteoinductivity *in vivo*. The mice were euthanized 2, 4, and 8 weeks later, and the membranes were gently removed from the defects. The samples were fixed in 4 % polymerized formaldehyde for 48 h and prepared for micro-CT, histology, and immunofluorescence assays.

2.12. Micro-CT

Mice were euthanized at 4 and 8 weeks post-implantation of BMC membranes. Subsequently, samples were scanned using a Skyscan micro-CT system (Bruker). To prevent dehydration, samples were kept in a humid environment during scanning. Morphometric analyses were conducted using CTAn software (Bruker), with grayscale settings ranging from 120 to 255 for optimal visualization. Three-dimensional reconstruction was performed to assess the bone microarchitecture, such as bone volume to total volume (BV/TV), bone mineral density (BMD), Tb. N (trabecular number), and Tb. Th (trabecular thickness), were calculated.

2.13. Histological analysis

The calvariae were decalcified in a solution of PBS containing 20 % ethylenediaminetetraacetic acid disodium (EDTA), with daily replacement of the solution. Following dehydration in a gradient of ethanol, the calvariae were embedded in paraffin and sectioned into slices 5 μm thick. These sections were then subjected to hematoxylin-eosin (H&E) staining, Masson staining, and immunohistochemical staining (OPN, IL6, IL10, and Piezo1), which were performed according to routine protocols [24].

2.14. RNA-seq and analysis

RAW 264.7 cells were cultured on the BMC membrane with or without LIPUS treatment for 3 days, and a parallel group of untreated cells on the culture dish was used as control. Then, total RNA extraction was performed, and the samples were forwarded to GENEWIZ (Azenta Life Sciences, Suzhou, China) for library preparation, RNA-seq, and subsequent data analysis. The raw sequencing data generated in this study have been deposited in the NCBI Gene Expression Omnibus (GEO) under the accession number GSE236912 and are publicly accessible. Differentially expressed genes (DEGs) were determined using criteria of $|\log2\text{fold change}| > 0.585$ and p-value < 0.05. Gene Ontology (GO) analysis was utilized to elucidate the gene regulatory network based on biological processes and molecular functions, while Kyoto Encyclopedia of Genes and Genomes (KEGG) pathway enrichment analysis was employed to identify significant pathways from the DEGs.

2.15. Intracellular calcium measurement

RAW 264.7 cells were seeded on the BMC membranes at a density of 5×10^5 cells per well in 24 well plates and cultured at 37 °C, followed by treatment with or without LIPUS. Cells were then washed with PBS three times and incubated with 2 μM of Fluo-4 AM (S1060, Beyotime, China) for 30 min at 37 °C. Intracellular Ca^{2+} levels were measured using a flow analyzer.

2.16. Statistical analysis

The results are presented as mean ± standard deviation. Data were obtained from a minimum of three independent experiments. Student's t-test was employed for comparisons between two groups, while one-way analysis of variance (ANOVA) followed by Tukey's multiple comparisons test was utilized for comparisons among multiple groups. All statistical analyses were conducted using GraphPad Prism v.5 software (GraphPad Software Inc.). Statistical significance was defined as $p < 0.05$.

3. Results

3.1. Characterization of the membranes

In the pre-experiments, the proportion of various constituents was refined by assessing the amounts of adherent cells, water contact angle, and pro-osteogenic effects (Fig. S1A). Cell adhesion is an important property of biomimetic periosteum. MWCNTs organic dispersion was firstly excluded due to the poor cell adhesiveness and Col was found to be indispensable to increasing initial cellular adhesion (Figs. S1B–C). Moreover, the 10%-MWCNT/BT/0.08g-Col group had a stronger pro-osteogenic effect with LIPUS stimulation; thus, the components were finally identified (Fig. S1D).

The XRD pattern revealed that the crystal structure of BT in the BT/MWCNT (BM) membrane was cubic, with sharp peaks at $2\theta = 31.4°$, 38.6°, and 44.9°, corresponding to the (110), (111), and (200) planes of crystalline BT (Fig. 1A). Moreover, the peak of MWCNT was covered by a broad peak corresponding to high-crystallinity BT (22.3°). In the MWCNT/Col (MC) membrane, 16.3° was the characteristic peak of Col, and 22.3° was the characteristic peak of MWCNTs. Notably, the peaks of BT in the BMC membrane were weakened, indicating that the membrane was covered by Col. Therefore, the Col outer layer of the membrane had higher biocompatibility, and BT and MWCNT particles were encapsulated inside, which promoted cell adhesion and survival. Raman spectroscopy (50–3500 cm^{-1}) was used to investigate the microstructural changes and electronic structure of the MWCNTs after the addition of BT and Col (Fig. 1B). The peaks at approximately 1323, 1387, and 2642 cm^{-1} belonged to the D, G, and D′-peaks of MWCNTs. The peak between 120 and 180 cm^{-1} was attributed to the stretching vibration of BT. Compared with the BM membrane, the intensity of MWCNTs in BMC was reduced, indicating that Col was coated on the surface of the MWCNTs which was consistent with the XRD results.

The water contact angles of BM, MC, and BMC were 119.5°, 53.38°, and 75.5°, respectively, indicating that Col significantly increased the hydrophilicity of the membranes (Fig. 1C). The surface morphology of various membranes was further observed by SEM (Fig. 1D). The BT particles in the BM membrane were uniformly embedded in the middle of the MWCNTs, but a few particles were slightly agglomerated. Col was deposited on the surface of MWCNTs within the MC membrane, resulting in a non-smooth surface texture. The BMC membrane combined the advantages of BM and MC. The particles were dispersed more evenly and tightly, which contributed to the stability and biocompatibility of the nanocomposites.

Fig. 1E and F showed the mechanical test results of the membranes. The Young's modulus and nanoindentation hardness values for BM, MC, and BMC were determined to be 0.44, 2.12, and 2.86 GPa, and 0.09, 0.10, and 0.30 GPa, respectively. This result suggested that the BMC membrane had a good capacity for mechanical support. Furthermore, the piezoelectric coefficients (d33) of the BM, MC, and BMC nanocomposite membranes were determined using piezoelectric force microscopy to be 0.6 pC/N, 0.63 pC/N, and 0.93 pC/N, respectively (Fig. 1G). We further confirmed the piezoelectricity by detecting the output voltage of the membranes with LIPUS stimulation (Fig. 1H). The output voltage of BMC with LIPUS stimulation was approximately 106 mV, which was significantly higher than MC (20.31 mV) and BM (45.78 mV) membranes. This result demonstrated that the BMC membrane possessed high electromechanical response sensitivity and could effectively generate electric signals for piezoelectric stimulation.

3.2. The BMC membrane exhibited good cytocompatibility to support cell proliferation and adhesion

The BMSC viability and adhesion experiments were first conducted, among BMC, BM and MC, to prove the superiority of BMC in biocompatibility (Fig. S2). And it showed that all three membranes exhibited good biocompatibility. However, the BM group showed lower CCK8

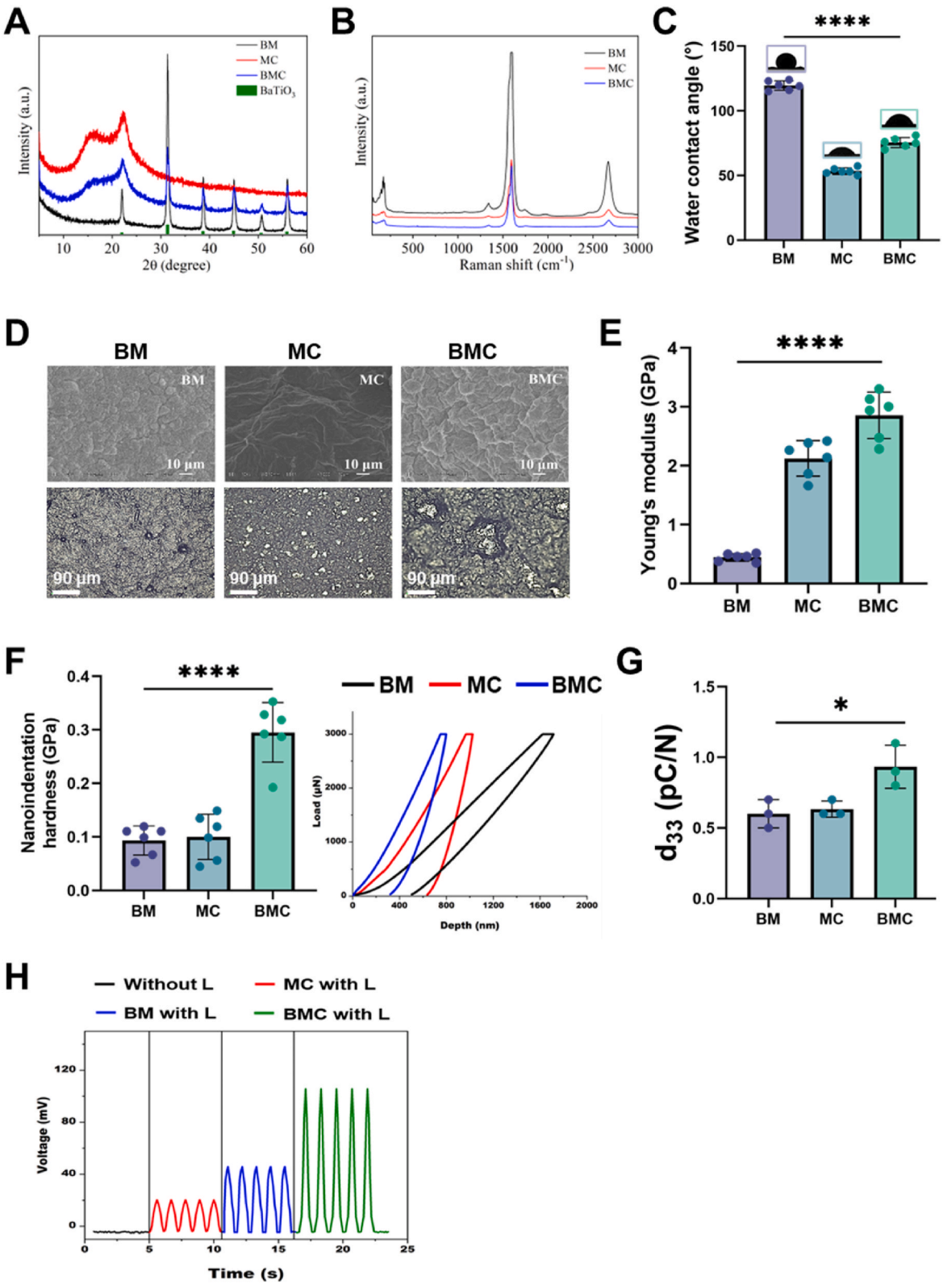

Fig. 1. Material Characterization.
(A) The XRD patterns of $BaTiO_3$, BM ($BaTiO_3$/MWCNTs), MC (MWCNTs/Col), and BMC ($BaTiO_3$/MWCNTs/Col) nanocomposite membranes are presented. **(B)** Raman spectra of BM, MC, and BMC nanocomposite membranes. **(C)** The water contact angle of various membranes; n = 6. **(D)** SEM images of BM, MC, and BMC nanocomposite membranes at different magnifications. **(E)** Young's modulus of the various membranes; n = 6. **(F)** Nanoindentation hardness of BM, MC, and BMC nanocomposite membranes; n = 6. **(G)** The piezoelectric coefficient d33 for the membranes; n = 3. **(H)** The output voltage of various membranes with or without LIPUS. L, LIPUS stimulation; *P < 0.05, ****P < 0.0001.

values, possibly due to the lack of collagen, resulting in fewer adhered cells. The CCK-8 assay showed that BMSCs cultured on the BMC membrane proliferated over time, while BMC + L could significantly stimulate cell proliferation (Fig. 2A). Live/dead staining results indicated some cell death in the BMC and BMC + L groups on Day 4 and Day 7, which might be caused by overdense cells (Fig. 2B and C). To explore the adhesion and spreading of BMSCs on the surface of the BMC membrane, the cells were fixed and stained on Day 3 for morphological observation. The results showed that BMSCs spread better in the BMC + L group than on bare BMC membranes (Fig. 2D and E).

3.3. BMC+L significantly promoted BMSC osteogenic differentiation

In terms of alkaline phosphatase (ALP), Runx2, OCN, and

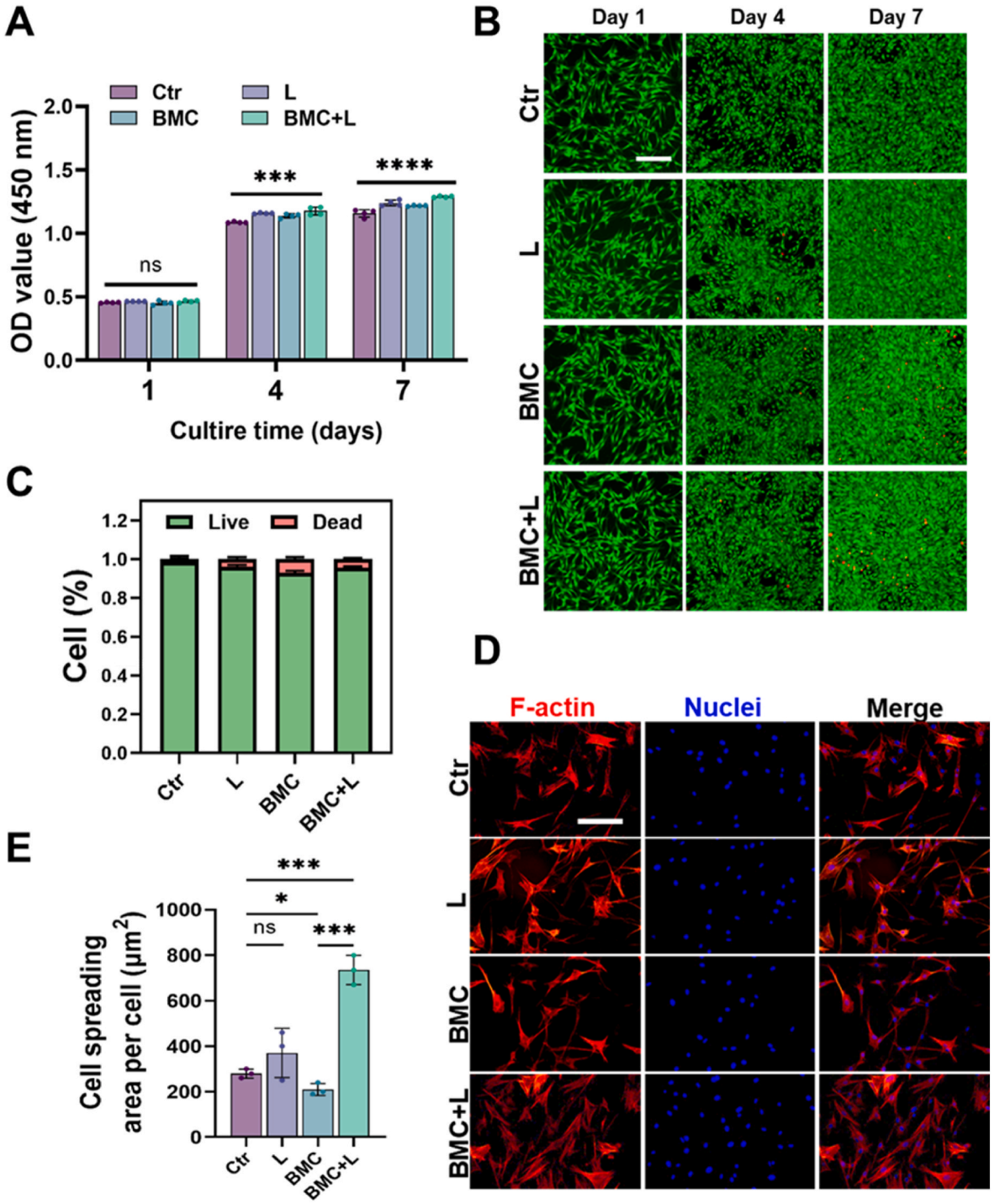

Fig. 2. BMSC viability and adhesion on the BMC membrane with or without LIPUS stimulation.
(A) Proliferation of BMSCs on the BMC membrane after 1, 4, and 7 days of culturing with or without LIPUS; n = 4. **(B)** Calcein AM (live)/PI (dead) staining images of BMSCs seeded on BMC membranes with or without LIPUS. Scale bar = 20 μm. **(C)** Statistical results of live/dead ratio calculated from the four groups. **(D)** Cell morphologies of BMSCs on the BMC membrane with or without LIPUS. Scale bar = 10 μm. **(E)** Cell spreading area of BMSCs; n = 3. L, LIPUS stimulation; ns = no significant, *P < 0.05, ***P < 0.001, ****P < 0.0001.

osteopontin (OPN) mRNA expression, the BMC membranes and LIPUS significantly promoted BMSC osteogenic differentiation after 7 and 14 days of stimulation compared with the control group (Ctr), respectively. Besides, this pro-osteogenic effect was further magnified by BMC + L, even compared with the BMC group ($P < 0.05$) (Fig. 3A and B). At the protein level, the ALP semiquantification and the immunofluorescence of OCN expression showed a similar tendency to the gene expression level (Fig. 3C and D).

3.4. BMC+L significantly promoted M2 polarization and further amplified the pro-osteogenic effects

To explore the immunomodulatory effects, RAW 264.7 cells were seeded on BMC membranes. BMC + L induced lower expression levels of M1-related genes (IL-1β, TNFα, and iNOS) but higher expression of M2-related genes (CD206 and Arg1) than BMC (Fig. 4A). Moreover, the immunofluorescence staining results showed that the level of iNOS in

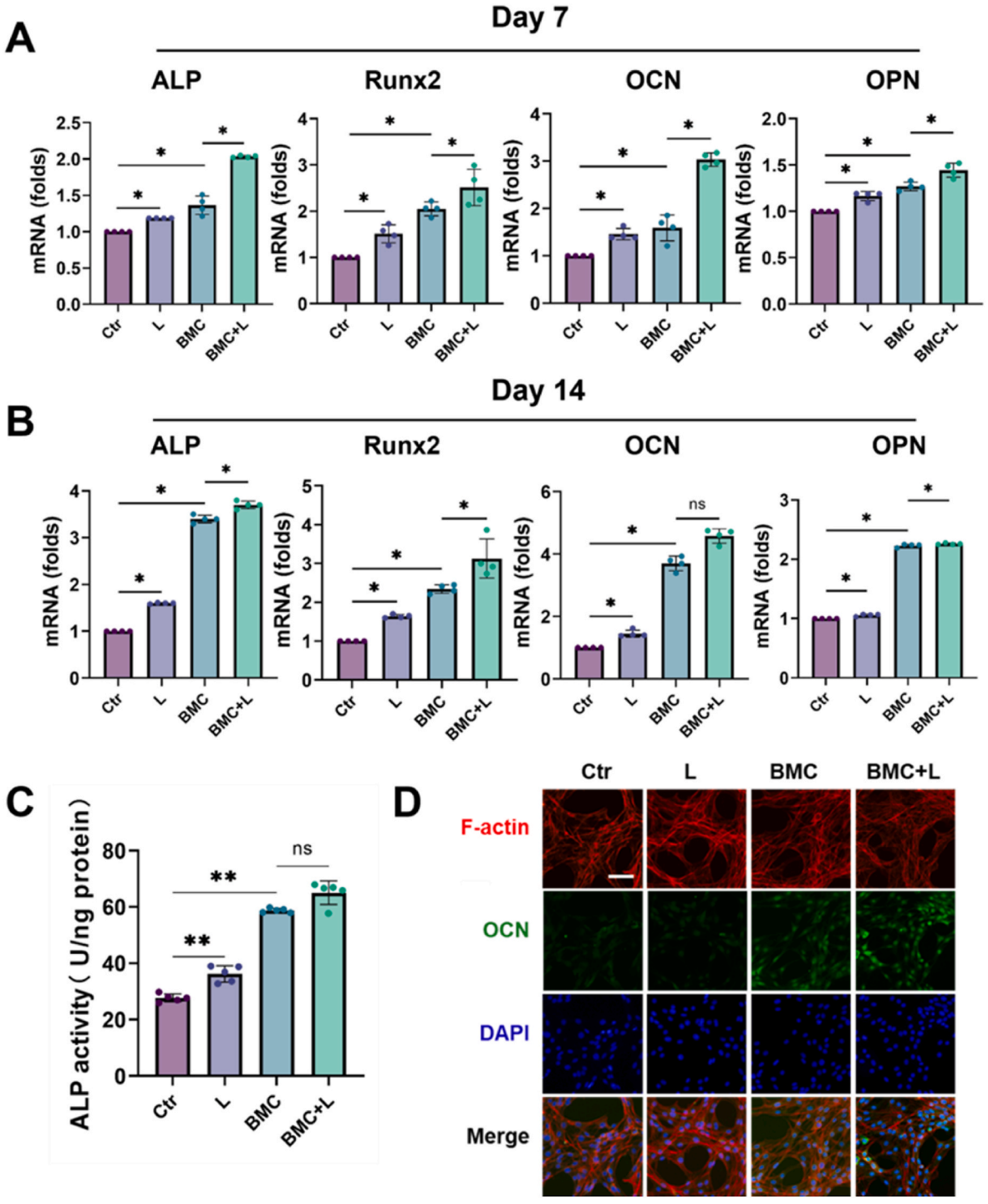

Fig. 3. Pro-osteogenic effects of BMC + L on BMSCs in vitro.
(A, B) Relative mRNA expression of osteogenesis-related genes, ALP, Runx2, OCN, and OPN after culturing on BMC membranes with or without LIPUS for 7 and 14 days, respectively; n = 4. **(C)** ALP activity quantitative analyses of BMSCs after 7-day culturing on BMC membranes with or without LIPUS; n = 5. **(D)** Fluorescence microscopy of OCN, F-actin, and nuclear staining (DAPI) of BMSCs cultured on BMC membranes with or without LIPUS. Scale bar = 10 μm. L, LIPUS stimulation; ns = no significant, *$P < 0.05$, **$P < 0.01$.

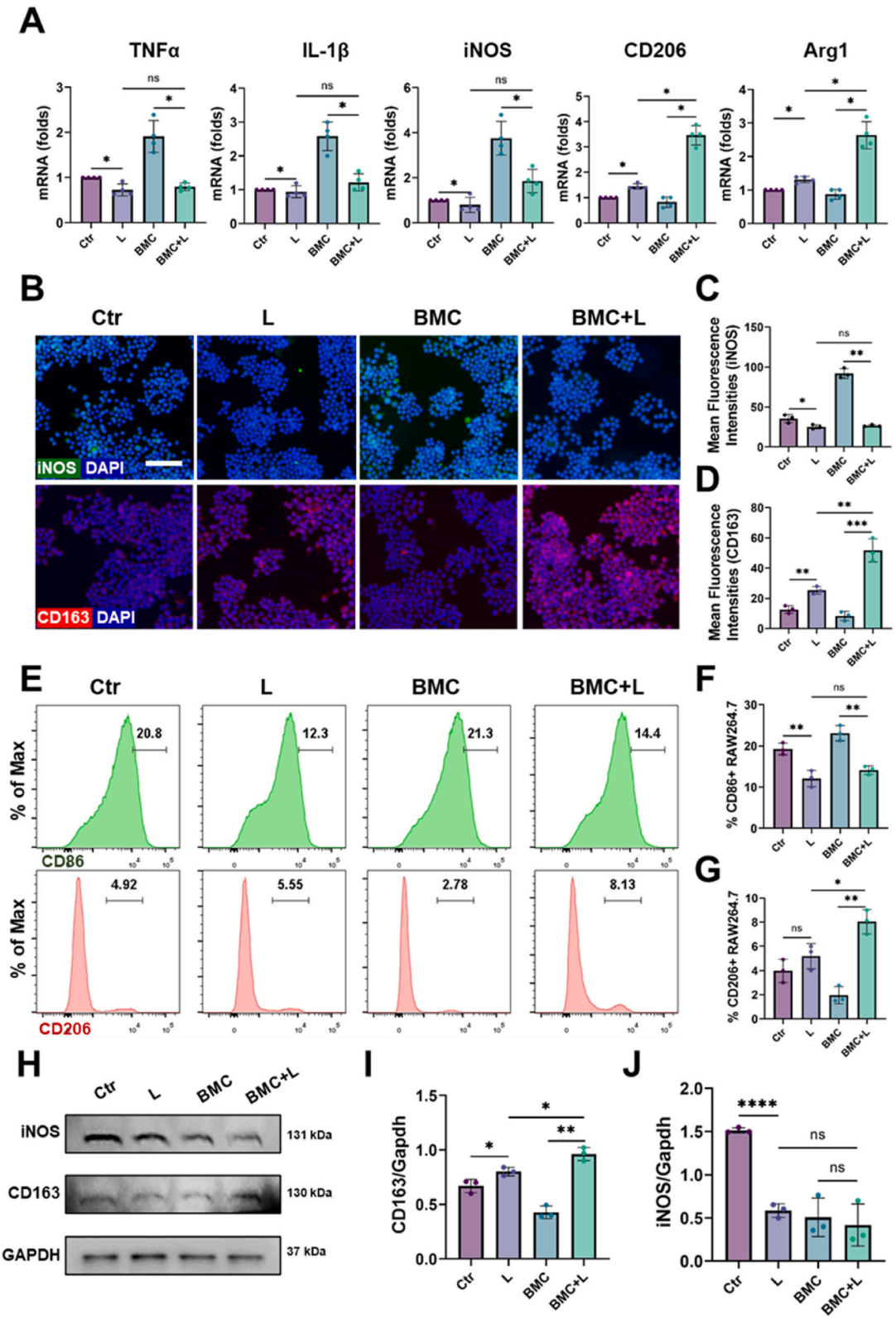

Fig. 4. Immunomodulatory effects of BMC + L on macrophages in vitro.
(A) Relative mRNA expression of inflammation-related genes, TNFα, IL-1β, iNOS, CD206, and Arg1 after culturing on BMC membranes with or without LIPUS for 3 days; n = 4. **(B–D)** Fluorescence microscopy and quantitative analysis of iNOS, CD163, and nuclear staining (DAPI) of macrophages cultured on BMC membranes with or without LIPUS; n = 3, Scale bar = 50 μm. **(E–G)** Polarization of macrophages was evaluated by expression of CD86 (M1) and CD206 (M2) using flow cytometry; n = 3. **(H–J)** Representative images and western blot analysis of iNOS and CD163; n = 3. L, LIPUS stimulation; ns = no significant, *P < 0.05, **P < 0.01, ***P < 0.001, ****P < 0.0001.

the BMC + L group was significantly lower than that in the BMC group (Fig. 4B and C). In contrast, the level of CD163 (M2 marker) in the BMC + L group was higher than that in the BMC group (Fig. 4B&D). Flow cytometric analysis further confirmed that BMC + L promoted macrophage polarization towards M2 type by increasing the proportion of $CD206^+$ cells (a marker of M2 macrophages) and inhibited M1 polarization by decreasing the proportion of $CD86^+$ cells (a marker of M1 macrophages) (Fig. 4E–G). The WB results also showed the same trend (Fig. 4H–J). These results indicated that BMC + L significantly induced M2 macrophage polarization and reduced M1 macrophage polarization compared with the bare BMC membranes.

Then, the effect of macrophages regulated by BMC membranes on BMSCs was further evaluated. First, macrophages were cultured on BMC membranes with or without L stimulation for 3 days. Then, the macrophage-conditioned medium was collected for BMSC culture (Fig. 5A). The expression levels of osteogenic gene markers, including ALP, Runx2, Col I, and OPN, were upregulated in BMSCs cultured in BMC + L medium compared with BMSCs cultured in BMC medium (Fig. 5B). Furthermore, ALP staining, ALP activity, and Alizarin red S (ARS) staining were performed. After incubation for 7 days, the colors of ALP staining of BMSCs in the BMC + L medium group were darker than those in the BMC groups, and the BMC + L medium group exhibited the highest ALP activity (Fig. 5C and D). After incubation for 14 days, obvious mineralized nodules were observed in the BMC + L medium group (Fig. 5C&E). As shown in Fig. 5F, the immunofluorescence staining results showed that the level of OPN in the BMC + L group was significantly higher than that in the BMC groups (Fig. 5G). The findings indicate a positive impact of BMC + L on the regulation of macrophages, leading to enhanced osteogenic differentiation of BMSCs. This effect is likely due to the immunomodulatory properties of BMC membranes activated by LIPUS, which in turn stimulate M2 macrophages to release cytokines related to osteogenesis.

3.5. BMC+L accelerated the repair of cranial bone defects by regulating the local inflammatory responses

A mouse cranial defect model was chosen to evaluate the regulatory effect of the BMC membranes on bone regeneration, which was analyzed 4- and 8 weeks post-surgery (Fig. 6A). Micro-CT analysis showed that the BV/TV, BMD, Tb·N, and Tb·Th in the BMC + L group were significantly higher than those of the other groups at 4 weeks post-surgery (Fig. 6B and C). The results at 8 weeks post-surgery showed a consistent trend. The H&E staining, shown in Fig. 6D, revealed that the defect areas in the control (Ctr) and LIPUS groups were filled with fibrous tissue at 4 weeks post-surgery, which indicated that such a region could not self-repair. Conversely, the defect region in the BMC group was filled with a small amount of new bone, whereas that in the BMC + L group was partly filled with new bone. Masson's trichrome staining was used to observe the repair of new bone tissue in the different groups. The BMC + L group had more well-developed bone than the LIPUS and BMC groups, which confirmed that BMC + L promoted the maturation of new bone. Besides, the osteogenic differentiation-related factor OPN was highly expressed in the BMC + L group, which indicated mineralization of the bone extracellular matrix (Fig. 6D). To further investigate the *in vivo* immunomodulatory activity of the BMC membranes, IL6 and IL10 were stained to identify the phenotype of macrophages in the bone defects 2 weeks after implantation. The expression of IL6 in the BMC + L group was lower than that in the other groups, indicating the attenuation of M1 macrophages in the defect region (Fig. 6E). Additionally, the expression of IL10 in the BMC + L group was higher than that in the other three groups, revealing the aggregation of M2 macrophages in the defect region. As Piezo1 is a vital regulator in the macrophage mechanosensing response, its expression was further evaluated. And the results showed that BMC + L significantly promoted the activation of Piezo1 (Fig. 6F). The consistent tendency of Piezo1 and IL10 might indicate the potential role of Piezo1 in the regulation of macrophage polarization.

3.6. Transcriptomic alterations of macrophages in BMC+L groups

RNA-seq was performed on RAW264.7 cells cultured in the control (Ctr), BMC, and BMC + L groups for 3 days, respectively. As shown in Fig. 7A, 14,080 genes were expressed in all three groups, and the number of genes exclusively expressed in each group was 32 (Ctr), 9 (BMC), and 15 (BMC + L). Moreover, the numbers of DEGs in the BMC group were 2296 (in comparison with the Ctr group) and 752 (in comparison with the BMC + L group) (Fig. 7B).

To explore the functions of polarized macrophages, GO functional enrichment analysis of DEGs between the BMC and BMC + L groups related to the cellular component, molecular function, and biological process categories was performed, and the results are shown in Fig. 7C. Many of the significantly affected GO terms in the cellular component category were related to voltage-gated ion channel complexes, such as cation channel activity and calcium ion homeostasis. Moreover, typical complexes closely associated with macrophage polarization were also enriched, e.g., complexes involved in the positive regulation of monocyte aggregation. For the molecular function category, several GO terms associated with macrophage function, including tubulin binding and extracellular matrix organization, were significantly enriched in genes expressed in the BMC + L group. Moreover, KEGG analysis was used to identify signaling pathways that were significantly enriched in DEGs between the BMC and BMC + L groups in detail (Fig. 7D). Among these pathways, the NF-kappa B signaling pathway, Toll-like receptor signaling pathway, and cytokine−cytokine receptor interaction were strongly associated with the polarization of macrophages. Based on the identified GO terms and KEGG analysis, we hypothesized that LIPUS exerted a synergistic effect involving both mechanical and electrical stimulation via the BMC membrane and therefore activated voltage-gated ion channels to effectively enhance M2 macrophage polarization.

As the expression of Piezo1 was upregulated in the BMC + L group in the cranial defect region (Fig. 6F), the regulatory role of Piezo1 remained to be investigated. To further determine the underlying mechanism, the expression of several DEGs was examined. Transcriptome analysis revealed that BMC + L upregulated Arg*1, Il10, and Il4*, indicating M2 polarization of RAW264.7 cells. The expression of *Piezo1* and *Calm1* was also upregulated in the BMC + L group (Fig. 7E). The immunofluorescence staining results showed that the expression of Piezo1 in the BMC + L group was significantly higher than that in the BMC and Ctr groups, which was further confirmed by the statistics for mean fluorescence intensities (Fig. 7F). Consistently, the intracellular Ca^{2+} concentration of RAW264.7 cells in the BMC + L group was significantly increased than that in other groups (Fig. 7G). Additionally, the application of a Piezo1 inhibitor (GsMTx4) significantly decreased the number of $CD163^+$ (M2 marker) macrophages, while the number of $iNOS^+$ (M1 marker) macrophages remained (Fig. 7H).

Combined with the decreased expression of *Tab2* and *Traf6* in the BMC + L group (Fig. 7E), it was indicated that the enhanced M2 polarization and inhibition of M1 polarization driven by BMC + L might occur through the activation of Piezo1 and the inhibition of the nuclear translocation of TLR, respectively (Fig. 7I).

4. Discussion

Piezoelectric biomaterials have the potential to surpass the limitations of existing electrical stimulation methods, as they can be activated wirelessly by external energy sources, such as ultrasound [25]. Employing piezoelectric biomaterials for wireless electrical stimulation signifies a revolutionary change in our approach to localized tissue stimulation and regeneration. Notably, the optimization of this strategy for clinical translation requires a systematic approach, including refining materials and energy sources, understanding biological complexities, implementing targeted therapy, and ensuring bio- and immunocompatibility while managing diverse *in vivo* scenarios [26]. Following the aforementioned methods, we fabricated the piezoelectric

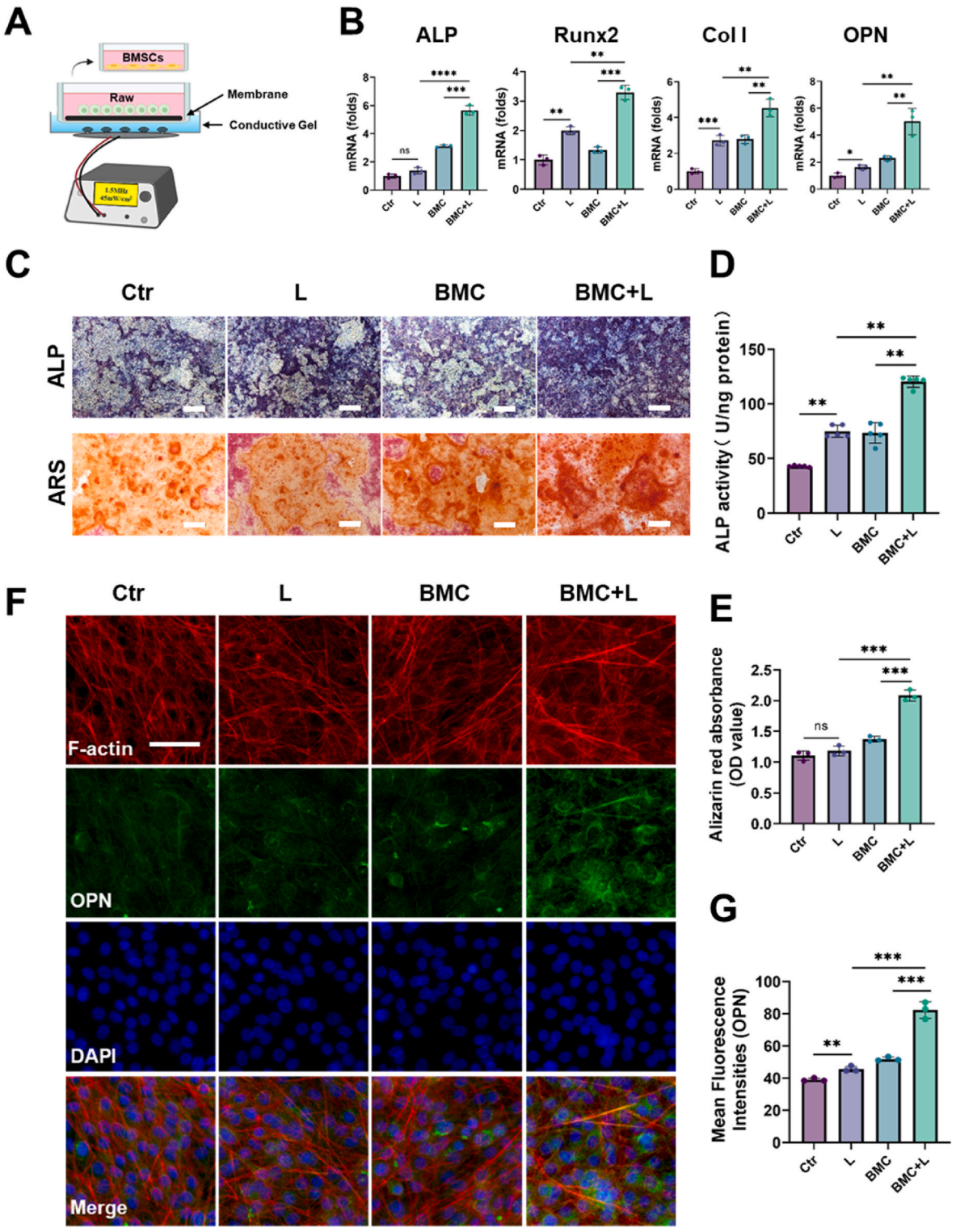

Fig. 5. Macrophages cultured on BMC membranes with LIPUS promoted osteogenic differentiation.
(A) Schematic illustration of the indirect coculture system of BMSCs and macrophages. **(B)** Osteogenesis-related gene expressions of ALP, Runx2, Col I, and OPN expressed by BMSCs after 7-day culture in the conditioned medium; n = 3. **(C)** ALP and Alizarin red S (ARS) staining after 7-day and 14-day cultures in the conditioned medium, respectively. Scale bar = 200 μm. **(D–E)** Quantitative analysis of ALP activity and ARS staining of BMSCs; n = 5 (D) or n = 3 (E). **(F–G)** Fluorescence microscopy and quantitative analysis of OPN after 7-day culture in the conditioned medium; n = 3, scale bar = 20 μm. L, LIPUS stimulation; ns = no significant, *P < 0.05, **P < 0.01, ***P < 0.001, ****P < 0.0001.

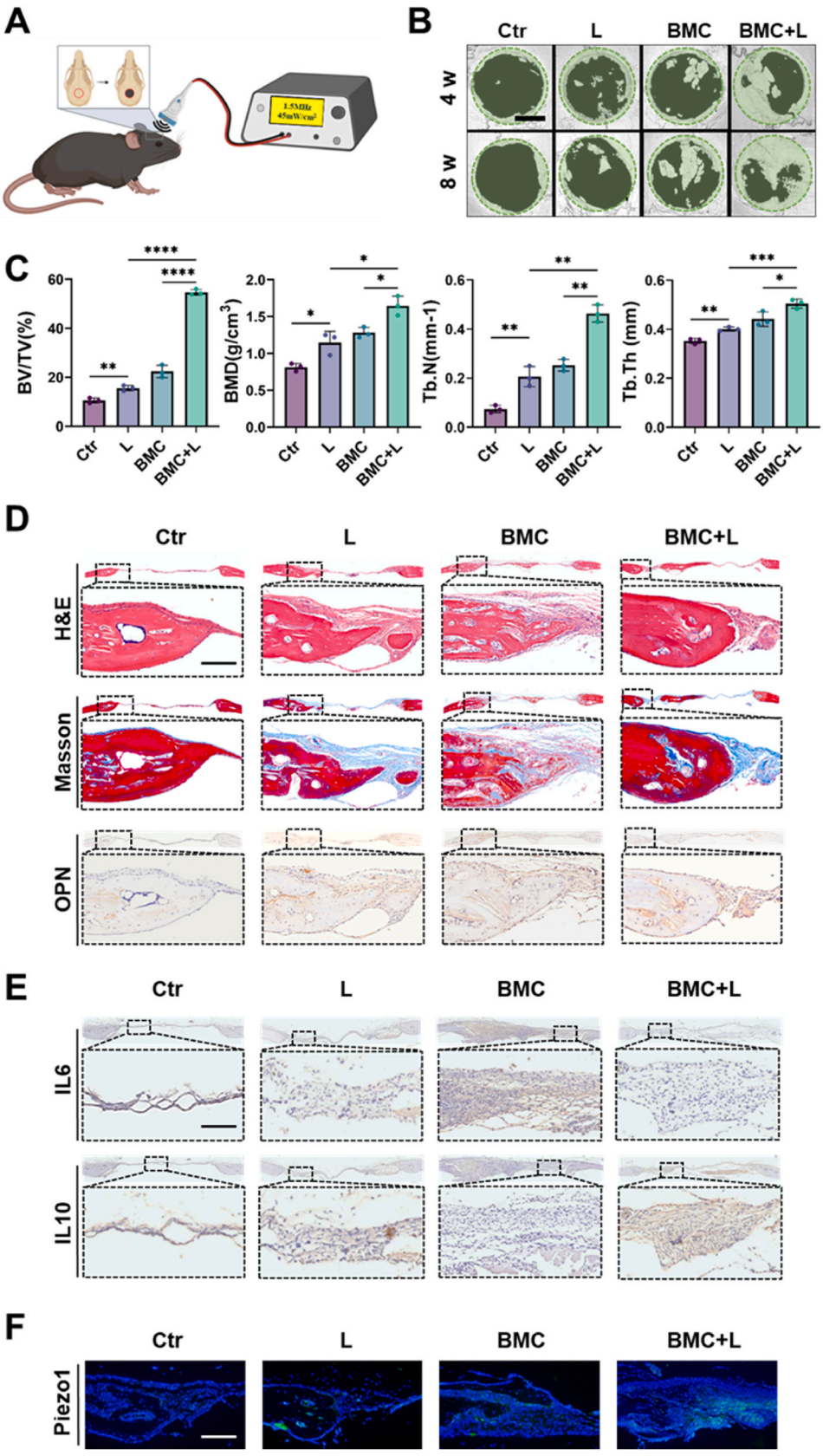

(caption on next page)

Fig. 6. The BMC + L promoted cranial bone regeneration.
(A) Schematic diagram of BMC + L treatment for mouse cranial bone defects. **(B)** Representative micro-CT images of calvarial defects with different treatments at 4 and 8 weeks after surgery. Scale bar = 2 mm. **(C)** The BV/TV, BMD, Tb. N, and Tb. Th. of the newly formed bone of all groups at week 4 after various treatments. **(D)** H&E, Masson, and OPN staining of calvarial bone defects from mice at week 4 after various treatments. Scale bar = 200 μm. **(E)** IL6 and IL10 staining of calvarial bone defects from mice at week 2 after various treatments. Scale bar = 200 μm. **(F)** Piezo1 fluorescence staining of calvarial bone defects from mice at week 2 after various treatments. Scale bar = 200 μm. L, LIPUS stimulation; *P < 0.05, **P < 0.01, ***P < 0.001, ****P < 0.0001.

BMC membranes and exploited LIPUS (1.5 MHz, 45 mW/cm^2, and 20 min/day) to recreate the endogenous electrical microenvironment of native bone. After that, the properties of the BMC membranes and the output voltage of the membranes with LIPUS stimulation were examined. Subsequently, how the synergistic effects of LIPUS and electrical signals regulate immune cells was explored. Finally, the regenerative effect of the BMC membrane with LIPUS stimulation was confirmed in a mouse cranial defect model.

Numerous attempts have been made to identify materials containing a microstructure comparable to periosteum or native bone [27]. Collagen, the primary protein found in bone, forms a hydrated fibrous network and exhibits beneficial biological properties as a naturally occurring polymer, offering numerous bioactive sites that promote cellular adhesion and regulate cellular differentiation [28,29]. Besides, the nanofibrous geometry of MWCNTs makes them notably interesting as a biomimetic analog for the fibrillary proteins of collagen, allowing them to function like collagen fibers during the deposition of bone matrix and to control the crystal nucleation events and growth of the inorganic component; hence, combining MWCNTs and Col was an advantageous strategy [30]. It is worth noting that MWCNTs can be used as implants in the form of artificial joints and other implants with no host rejection response [31]. On account of their high tensile strength, MWCNTs can also serve as bone substitutes when filled with calcium and shaped or arranged to mimic bone structure [32]. Moreover, cellular adhesion and proliferation can be enhanced with MWCNT composites, and therefore, MWCNTs have been integrated into Col to generate the biomimetic periosteum in this study [33]. On the other hand, living bone generates electrical signals by the application of mechanical stress due to the presence of piezoelectric collagen [34]. Studies have demonstrated that BT ceramics have desirable biocompatibility and bioactivity, and the piezoelectric potential of BT could promote apatite deposition, cell differentiation, and bone formation [35]. In this study, water-soluble MWCNTs, Col, and BT were utilized to fabricate the piezoelectric membranes, which were then experimentally verified with ideal physicochemical properties and biocompatibility.

The microstructure of BMC membranes was initially evaluated to ensure long-term cell adhesion and viability, showing that the particles were evenly and tightly dispersed, which enhanced the stability and biocompatibility of the nanocomposites (Fig. 1D). However, several potential challenges associated with the microstructure may impact the long-term biocompatibility. Particle agglomeration is a major issue, as micro- or nanoparticles can cluster, leading to uneven surface properties and disrupting uniform cell adhesion. This can result in areas with varying mechanical properties, hindering consistent cell growth [36]. Additionally, pore size and distribution are critical; improper pore sizes can impair nutrient exchange and waste removal, negatively impacting cell health [37]. Surface chemistry is another concern, as any changes or degradation in surface properties can affect cell adhesion and proliferation [38]. Addressing these challenges is crucial for ensuring the long-term effectiveness and biocompatibility of membrane-based cell support systems.

The BMC membrane displayed elevated values of Young's modulus and nano hardness, enhancing its support in the friction process [39]. Additionally, alongside their outstanding mechanical properties, the piezoelectric properties of different membranes underwent further evaluation. The piezoelectric coefficient of the BMC membrane is approximately 0.93 pC/N, which is comparable to that of natural bone, which can reach up to 0.7 pC/N [12,40]. The similar piezoelectric coefficients suggest that the BMC membrane can effectively emulate the electrical stimulation of natural bone during mechanical stress, which is important for bone regeneration and healing. By closely replicating natural bone's piezoelectric response, the BMC membrane may enhance cellular activities like proliferation and differentiation, improving integration and functionality in bone tissue engineering [41]. This makes it a promising candidate for biomedical applications in bone regeneration and repair. With LIPUS stimulation, the output voltage of the BMC membrane significantly increased, indicating its high sensitivity to electromechanical response.

LIPUS is an ultrasound wave with a frequency of 1–3 MHz and an intensity of <1 W/cm^2 that can provide low-intensity mechanical stimulation, instigate micro-mechanical interactions with cells, trigger intracellular biochemical effects, and ultimately facilitate tissue repair and regeneration [42]. Numerous studies have demonstrated that LIPUS can enhance cell survival [43,44]. LIPUS induces mechanical stress and micro-vibrations, increasing cell membrane permeability and nutrient exchange [45]. It has been reported that LIPUS promotes the synthesis and secretion of the extracellular matrix and reduces cell apoptosis by upregulating SOX9 expression [43]. Additionally, LIPUS initially upregulates heat-shock proteins 90 and phosphorylation of Smad1 and Smad5, encouraging cell viability and proliferation [44]. LIPUS also exerts anti-inflammatory effects by reducing pro-inflammatory cytokines and increasing anti-inflammatory ones, thereby helping to decrease cell death caused by inflammation [46]. Finally, LIPUS could enhance calcium influx, serving as a secondary messenger in survival signaling pathways [47].

An analysis of the utilization of LIPUS in the field of bone tissue engineering has revealed that LIPUS exhibited efficacy in improving osteogenic differentiation, mineralization, the volume of newly formed bone, and osseointegration [48]. Although LIPUS has demonstrated great efficacy as an independent treatment, its potential for improving bone formation could be further augmented through its integration with other strategies. Specifically, LIPUS has been suggested to have synergistic effects in combination with piezoelectric effects [49]. Liu et al. demonstrated that BMSCs cultured on scaffolds coated with BT exhibited elevated ALP activity and upregulated the expression of ALP, RUNX2, and Col I following 7 and 14 days of LIPUS stimulation in comparison to cells cultured on uncoated titanium scaffolds [50]. Similarly, Cai et al. found that osteogenesis was promoted by the use of piezoelectric BT/TC4 material with synergistic LIPUS loading [12]. Genchi et al. also proved that ultrasound could activate piezoelectric composite films composed of P(VDF-TrFE)/boron nitride nanotubes and promote the differentiation of human SaOS-2 osteoblast-like cells [51]. In our study, it was also suggested that LIPUS could significantly magnify the pro-osteogenic effects of BMC membranes on BMSCs due to the synergistic effect of both mechanical and electrical stimulation.

In addition to directly promoting osteogenesis, LIPUS, when combined with piezoelectric material stimulation, also plays a role in modulating macrophage responses, further indirectly promoting bone formation. Liu et al. reported that localized electrical signals generated from a piezoelectric β-PVDF membrane stimulated by ultrasound promoted M1 macrophage polarization and enhanced tumor immunotherapy [21]. Previous research demonstrated that LIPUS markedly inhibited the expression of M1 macrophage-related genes and significantly promoted the expression of M2 macrophage-related genes, exhibiting an anti-inflammatory effect [52,53]. Deng et al. reported that the polarized $BaTiO_3$/P(VDF-TrFE) nanocomposite membrane

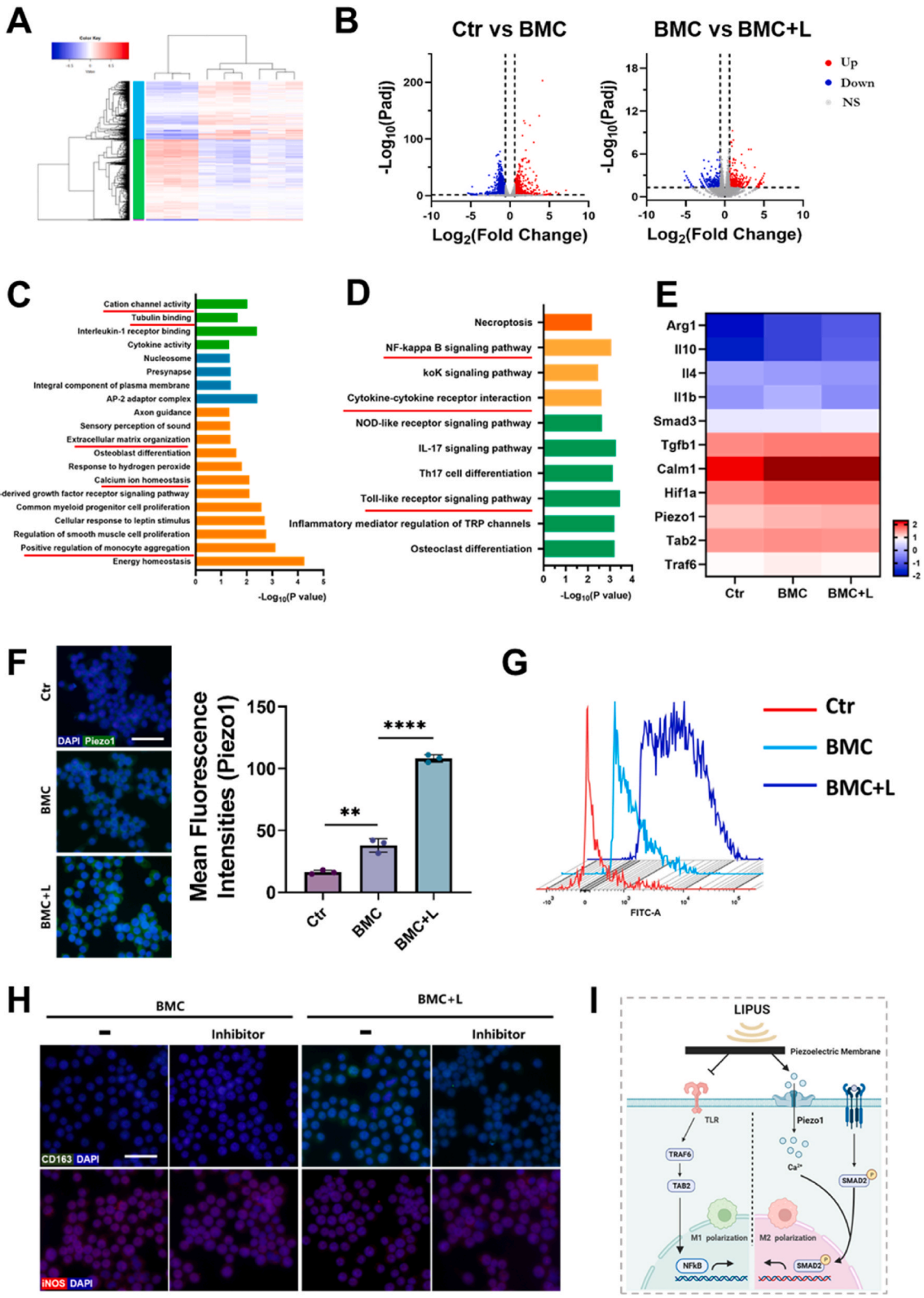

Fig. 7. Polarization mechanism of the piezoelectric effect.

(A) Heatmap visualization of RNA-seq results and cluster analysis of differentially expressed genes (DEGs). Red indicates upregulated genes; blue indicates downregulated genes. **(B)** Volcano plots of the gene expression profile in macrophages: Ctr versus BMC and BMC versus BMC + L groups; up, ns, and down indicate upregulated genes, nonsignificant genes, and downregulated genes, respectively. **(C)** Gene ontology analysis of all genes in macrophages cultured on BMC membranes with LIPUS stimulation versus without LIPUS stimulation. **(D)** Enriched KEGG pathways of BMC versus BMC + L. **(E)** Heatmap of typical DEGs associated with macrophage polarization. **(F)** Immunofluorescence images and quantification analysis of Piezo1 expression in macrophages. Scale bar = 50 μm. **(G)** Detection of intracellular calcium content by flow cytometry. **(H)** Immunofluorescence analysis of CD163 and iNOS expression in macrophages under various treatments. Scale bar = 30 μm. **(I)** Schematic summary of the macrophage polarization pathways induced by BMC + L. L, LIPUS stimulation; **P < 0.01, ****P < 0.0001.

transformed M1 macrophages into M2 macrophages and promoted bone repair *in vivo* [54]. In our study, the results also suggested that LIPUS, in synergy with the BMC membrane, can collectively promote macrophage M2 polarization, thereby amplifying the pro-osteogenic effects.

Ultrasound parameters play a key role in ultrasound stimulation. However, most of the studies reported above are affected by such issues: some fail to disclose the complete set of ultrasound parameters utilized, and others rely on sonication baths that result in inconsistent exposure conditions. In such cases, it is impossible to deduce or precisely quantify the ultrasonic dose the samples receive, leading to a lack of precise data on the effects of the treatment. Consequently, mainly due to the absence or insufficiency of detailed information regarding the ultrasonic source and the acoustic propagation dynamics within the experimental configuration, results may not be comparable and repeatable by others. In our study, the ultrasound intensity was set to 45 mW/cm^2, with an ultrasonic frequency of 1.5 MHz, a pulse repetition rate of 1 kHz, and a pulse duty cycle of 20 %. The ultrasound intensity (UI) was calculated using a formula (UI = 8.1 × voltage (V) [2] *pulse duty cycle), which has been confirmed to be effective in promoting bone defect repair (patent granted) [10,55,56]. Another innovative aspect of this study lies in the ultrasound loading method. The cells were cultured on a soft silicone membrane, with the ultrasound conduction medium being conductive gel. This combination ensured a more uniform distribution of ultrasound intensity across the cells.

Ion channels are membrane proteins crucial for altering membrane potentials, and they have been shown to play a role in modulating the environment of mononuclear immune cells by influencing inflammatory or anti-inflammatory cascades [57,58]. Piezo1, functioning as a mechanically sensitive ion channel with a nonselective cation channel, is primarily expressed in tissues not involved in sensory perception, particularly those influenced by contact fluid pressure and flow [59]. It plays a crucial role in cellular processes such as differentiation and homeostasis by transforming external physical stimuli into physiological signals, acting as a pressure sensor, detecting electric signals, and initiating Ca^{2+} influx [60–63]. Piezo1 is the most highly expressed mechanosensitive ion channel in macrophages and a vital regulator in the macrophage mechanosensing response [64]. It has been observed that LIPUS could activate Piezo1 and enhance Piezo1-induced calcium influx [65]. Moreover, electrically activated cellular behaviors are connected to signaling pathways that involve calcium influx, primarily relying on Piezo1 [66]. The expression of Piezo1 was further evaluated following observed changes in the expression of IL6 and IL10 in the bone defects in this study. The results indicated the level of Piezo1 activation stimulated by the BMC membrane under LIPUS stimulation was significantly higher than that under pure LIPUS stimulation, which suggested that the BMC membrane acted as a transducer, amplifying the electrical signals. Thus, we continued to explore the molecular mechanisms by which BMC + L regulated macrophage phenotypes through Piezo1.

The RNA sequencing results revealed a significant upregulation in the expression of *Calm1* and *Piezo1* in the BMC + L group (Fig. 7E&F). The calcium-binding protein CALM-1 can regulate cell motility, differentiation, and proliferation by targeting calcium ion transport [67]. Moreover, Piezo1 can transduce LIPUS-induced signals into intracellular calcium, and the influx of Ca^{2+} serves as a second messenger to trigger downstream cellular signaling processes, which was consistent with our results (Fig. 7F&G) [68]. To further elucidate the role of Piezo1 in the mechanism of BMC + L-induced M2 polarization, we pre-incubated cells with a Piezo1 inhibitor. And the results indicated that BMC + L-induced M2 polarization depends on Piezo1 activation (Fig. 7H). Zhang et al. found that residual bone marrow macrophages responded to mechanical stretching by activating Piezo1, resulting in an M2-like phenotype [69]. Cai et al. concluded that mechanical tension induced calcium influx and macrophage polarization toward M2 via Piezo1, which in turn supported BMSC osteogenesis [70]. In contrast, Jiang et al. reported that macrophages are polarized from the M0 to M2 phenotype by blocking the Piezo1-AP1-CCL2 signaling pathway [71].

Besides, the RNA sequencing results also showed a significant downregulation in the expression of *TRAF6* in the BMC + L group. TRAF6, a TLR signaling adaptor, mediates a wide array of protein-protein interactions and serves as a mediator of interleukin-1 receptor (IL-1R)-mediated activation of NF-κB [72]. TRAF6 has since been identified as an actor downstream of multiple receptor families with immunoregulatory functions. Kim et al. indicated that interruption of TRAF6 ubiquitination would induce activation of TAK1 activity in the TLR (Toll-like receptor)-mediated signaling cascade, leading to TNF-α production [73]. Sun et al. demonstrated that a shift from pro-M2 macrophages to pro-M1 macrophages was closely related to decreased inhibition of the TRAF6/NF-κB pathway [74]. Ren et al. also reported that downregulation of TRAF6 reversed the promoting effect of M1 macrophage polarization [75].

In conclusion, the mechanism of M2 polarization mediated by BMC + L is likely attributed to the downregulation of Tab2and Traf6, which inhibits inflammation by suppressing TLR nuclear translocation. Simultaneously, the upregulation of Piezo1 was also indispensable for promoting M2 polarization (Fig. 7I).

5. Conclusion

Herein, we fabricated the biomimetic BMC periosteum and utilized the synergistic effect of LIPUS to enhance bone regeneration. Activated by LIPUS, the piezoelectric BMC membrane was able to recreate the endogenous electrical microenvironment similar to that of native bone. The wireless-generated electrical signals, along with the mechanical signals induced by LIPUS, were transferred to macrophages, leading to the activation of Ca^{2+} influx through Piezo1 channels. Our research introduces a promising co-engineering strategy for bone regeneration by integrating a novel biomimetic periosteum with the synergistic effects of ultrasound, thereby enhancing the electrical environment and modulating macrophage polarization.

CRediT authorship contribution statement

Ting Jiang: Data curation, Conceptualization. **Fei Yu:** Funding acquisition, Formal analysis. **Yuqi Zhou:** Software, Methodology. **Ruomei Li:** Validation, Methodology. **Mengting Zheng:** Software, Resources. **Yangyang Jiang:** Supervision, Data curation. **Zhenxia Li:** Validation, Investigation. **Jun Pan:** Supervision, Resources. **Ningjuan Ouyang:** Writing – review & editing, Writing – original draft.

Declaration of competing interest

The authors declare that they have no known competing financial interests or personal relationships that could have appeared to influence the work reported in this paper.

Data availability

Data will be made available on request.

Acknowledgments

This work was supported by the National Natural Science Foundation of China (82101047), and Fundamental Research program funding of Ninth People's Hospital affiliated with Shanghai Jiao Tong University School of Medicine (JYZZ138, JYZZ085B). Additional support was received from the Shanghai Key Laboratory of Translational Medicine on Ear and Nose Diseases (14DZ2260300), Shanghai's Top Priority Research Center (2022ZZ01017), and CAMS Innovation Fund for Medical Sciences (CIFMS, 2019–12M-5-037).

Appendix A. Supplementary data

Supplementary data to this article can be found online at https://doi.org/10.1016/j.mtbio.2024.101147.

References

[1] J. Nan, et al., Front. Bioeng. Biotechnol. 10 (2022) 1038250.
[2] X. Zhang, et al., Clin. Orthop. Relat. Res. 466 (8) (2008) 1777.
[3] G. Yang, et al., Biomaterials 268 (2021) 120561.
[4] L. Liu, et al., Adv. Healthcare Mater. 10 (21) (2021) e2101195.
[5] P. Wang, et al., Front. Bioeng. Biotechnol. 10 (2022) 988300.
[6] G. Thrivikraman, et al., ACS Appl. Mater. Interfaces 7 (41) (2015) 23015.
[7] W. Zhao, et al., Bone 144 (2021) 115825.
[8] M.B. Bhavsar, et al., Eur. J. Trauma Emerg. Surg. 46 (2) (2020) 245.
[9] M. Liu, et al., Adv. Mater. (2024) e2313672.
[10] J. Li, et al., Ultrasonics 118 (2022) 106561.
[11] B. Fan, et al., Bioact. Mater. 5 (4) (2020) 1087.
[12] K. Cai, et al., Bioact. Mater. 6 (11) (2021) 4073.
[13] R.N. Azadani, et al., Int. J. Biol. Macromol. 260 (Pt 1) (2024) 129407.
[14] H. Li, et al., ACS Appl. Mater. Interfaces 13 (21) (2021) 25290.
[15] B. Murugesan, et al., Mater. Sci. Eng. C 111 (2020) 110791.
[16] B. Tandon, et al., Acta Biomater. 73 (2018) 1.
[17] J. Wu, et al., Regen Biomater 8 (6) (2021) rbab065.
[18] J. Zhang, et al., Adv. Mater. 34 (36) (2022) e2202044.
[19] W. Qiao, et al., Nat. Commun. 12 (1) (2021) 2885.
[20] Y. Li, et al., Bioact. Mater. 18 (2022) 213.
[21] Y. Kong, et al., Adv. Sci. 8 (13) (2021) 2100962.
[22] L. Wang, et al., Gene Dev. 31 (20) (2017) 2056.
[23] C.-F. Chang, et al., Neurobiol. Dis. 103 (2017) 54.
[24] F. Yu, et al., ACS Nano 16 (1) (2022) 755.
[25] T. Vinikoor, et al., Nat. Commun. 14 (1) (2023) 6257.
[26] A. Cafarelli, et al., ACS Nano 15 (7) (2021) 11066.
[27] Z. Jing, et al., Ann. Biomed. Eng. 45 (9) (2017) 2075.
[28] Y. Chen, et al., Acta Biomater. 67 (2018) 341.
[29] L. Liu, et al., J. Mater. Chem. B 8 (3) (2020) 558.
[30] A.S. Herford, et al., J. Craniofac. Surg. 24 (4) (2013).
[31] L. Bao, et al., Nano Today 49 (2023) 101784.
[32] T.R. Nayak, et al., ACS Nano 4 (12) (2010) 7717.
[33] T.C. Suh, et al., ACS Omega 7 (23) (2022) 20006.
[34] Y. Huang, et al., Colloids Surf. B Biointerfaces 204 (2021) 111785.
[35] H. Wu, et al., Biomaterials 293 (2023) 121990.
[36] M.H.U. Rehman, et al., Polymers 15 (3) (2023).
[37] T.-T. Nguyen, et al., Biomater. Res. 26 (1) (2022) 21.
[38] K. Sun, et al., Bioact. Mater. 8 (2022) 253.
[39] S. Wei, et al., Materials 15 (15) (2022).
[40] Y. Zhang, et al., Mater. Sci. Eng., C 39 (2014) 143.
[41] X. Dai, et al., Int. J. Nanomed. 17 (2022) 4339.
[42] X. Jiang, et al., IEEE Trans. Biomed. Eng. 66 (10) (2019) 2704.
[43] W. Ding, et al., Int. J. Clin. Exp. Pathol. 13 (4) (2020) 810.
[44] M. Miyasaka, et al., Tissue Eng. 21 (23–24) (2015) 2829.
[45] W. Jiang, et al., Sci. Rep. 6 (2016) 22773.
[46] X. Li, et al., Cell. Mol. Biol. Lett. 28 (1) (2023) 9.
[47] H. Yao, et al., J. Nanobiotechnol. 20 (1) (2022) 378.
[48] H. Lu, et al., Am. J. Sports Med. 34 (8) (2017) 1287.
[49] C. McCarthy, G. Camci-Unal, Micromachines 12 (12) (2021).
[50] W. Liu, et al., J. Biomater. Appl. 35 (4–5) (2020) 544.
[51] G.G. Genchi, et al., Nanomedicine 14 (7) (2018) 2421.
[52] S.A.A. Gouda, et al., Life Sci. 314 (2023) 121338.
[53] B. Zhang, et al., Autophagy 16 (7) (2020) 1262.
[54] X. Dai, et al., Bioact. Mater. 6 (7) (2021) 2029.
[55] L. Xia, G. S, B. Fang, W. Shi, L. Li, Z. Chen, R. Chen, Q. You, L. Yuan, N. Ouyang, X. Zheng, Z. Li, A Control Method, System, and Device for Accelerating Orthodontic Tooth Movement Using Ultrasound: Chinese Invention Patent China, 2021. CN202011031537.6.
[56] L. Xia, G. S, B. Fang, W. Shi, Z. Chen, L. Li, L. Yuan, N. Ouyang, X. Zheng, Z. Li, R. Chen, Q. You, An ultrasonic generator for accelerating orthodontic tooth movement: Chinese Utility Model Patent. China, 2021. CN202022152701.0.
[57] L. Abdul Kadir, et al., Front. Physiol. 9 (2018).
[58] S. Feske, et al., Annu. Rev. Immunol. 33 (1) (2015) 291.
[59] H. Kang, et al., Am. J. Physiol. Cell Physiol. 316 (1) (2019) C92.
[60] T. Zhou, et al., Elife (2020) 9.
[61] S.A. Gudipaty, et al., Nature 543 (7643) (2017) 118.
[62] S.M. Cahalan, et al., Elife (4) (2015).
[63] Z.M. Zhang, et al., Adv. Healthcare Mater. (2023) e2300713.
[64] A.G. Solis, et al., Nature 573 (7772) (2019) 69.
[65] Z. Jiang, et al., Advanced Science (Weinheim, Baden-Wurttemberg, Germany), 2024 e2305489.
[66] T.-H. Kim, et al., Biomaterials 275 (2021) 120948.
[67] M. Yao, et al., Front. Genet. 12 (2021) 793508.
[68] G. Zhang, et al., Bone Res 9 (1) (2021) 16.
[69] X. Zhang, et al., Theranostics 12 (4) (2022) 1621.
[70] G. Cai, et al., Cell Prolif. (2023) e13440.
[71] J. Jiang, et al., Explorations 3 (2) (2023) 20220147.
[72] M.C. Walsh, et al., Immunol. Rev. 266 (1) (2015) 72.
[73] S.H. Kim, et al., Biomed. Pharmacother. 155 (2022) 113688.
[74] J. Sun, et al., Exp. Neurol. 362 (2023) 114295.
[75] W. Ren, et al., Mol. Cell. Biochem. 476 (1) (2021) 471.